Hybrid model of atmospheric pressure $Ar/O_2/TiCl_4$ radio-frequency capacitive discharge for TiO_2 deposition

A. Leblanc,[1] Ke Ding,[2] M. A. Lieberman,[3,a)] De Xin Wang,[4] Jing Zhang,[4] and Jian Jun Shi[4]
[1]*ENS Cachan, UPMC, Paris, France*
[2]*College of Science, Donghua University, Shanghai 201620, China*
[3]*Department of Electrical Engineering, University of California, Berkeley, California 94720, USA*
[4]*College of Materials Science and Engineering, Donghua University, Shanghai 201620, China*

(Received 21 January 2014; accepted 30 April 2014; published online 12 May 2014)

A hybrid global-analytical model of an atmospheric pressure radio-frequency driven capacitive discharge is applied to determine the plasma conditions for TiO_2 film deposition. The feed gas is mainly argon with a small fraction of O_2 and a smaller fraction of $TiCl_4$. Variations of the discharge parameters and species densities with O_2 concentration, discharge power, and flow rate are determined. A simplified chemistry model is developed and compared with the simulation results, showing good agreement. For a base case with $Ar/O_2/TiCl_4$ flow rates of 203/30/0.17 sccm, the results indicate that a minimum O_2 fraction of 7.3×10^{-4} is required for pure (un-chlorinated) TiO_2 film deposition that the active precursor species is TiO_2Cl_3, with subsequent abstraction of Cl atoms by dissociative electron attachment and that the deposition rates are around 1 nm/s. © *2014 AIP Publishing LLC*. [http://dx.doi.org/10.1063/1.4876062]

I. INTRODUCTION

Anatase self-connected TiO_2 films with exposed 001 reactive facets and oxygen defects are highly desirable for scientific and technical applications,[1–3] possessing interesting photo-, electro-, magnetic-, chemical-, catalyst-, and cytokine-effects, with possible applications in photonics crystals, photo/electrochromic devices, gas sensors, and spintronic devices. There are also applications to anticancer or gene therapies,[4,5] and these films are especially attractive for photocatalysts in solar cells for the production of electric energy or hydrogen.[6]

It was recently demonstrated[7] that a self-confined growth and connection of anatase single crystal sheets with two exposed 001 crystal facets can be completed simultaneously in a reactive, atmospheric pressure TiO_2O_2/Ar radio frequency (rf) plasma discharge. The experimental configuration is an rf capacitive discharge driven at 13.56 MHz with approximately 100 W of input power. The geometry is coaxial, with an inner copper electrode diameter of 10 mm, an outer copper electrode diameter of 13 mm, and an active discharge length of 2 cm. The substrates are placed at various locations along the inner surface of the outer tube wall. The feed gas mixture of $Ar/O_2/TiCl_4$ (base case 203/30/0.17 sccm at initial temperature 300 K) flows from the inlet at one end of the tube to the outlet at the other end. The typical film growth time is 1–2 h, and the deposition rates are non-uniform along the tube. In one experiment, 0.14 nm/s was measured in the middle of the active discharge region, 0.9 nm/s at the tube exit, and 0.6 nm/s a few centimeters into the afterglow.[7] The deposited films are nano-crystalline and display a strong white photoluminescence, whose intensity is comparable to that of commercial fluorescent lamp coatings.

Thermally produced titanium dioxide is of great commercial importance for use as a pigment, catalyst support and photocatalyst. In the current production method, $TiCl_4$ is oxidized at high temperatures (1500–2000 K) and pressures (300 kPa) in a pure oxygen plasma or flame to produce TiO_2. In the last decade, the chemistry and gas phase rate coefficients for the high-temperature oxidation of $TiCl_4$ to produce TiO_2 have become fairly well known, and equilibrium calculations have been performed to identify which intermediates and precursors are most important in the high temperature process.[8–13] However, there have been no simulations to our knowledge of the production of TiO_2 films in low temperature, atmospheric pressure $Ar/O_2/TiCl_4$ plasmas.

In this work, we perform such simulations using a hybrid analytical-numerical global model of an atmospheric pressure, rf-driven capacitive discharge. A detailed description of the model is given in Ref. 15. The feed gas is assumed to be a rare gas with small admixtures of other gases. The electrical characteristics are determined analytically using a symmetric, current-driven homogeneous discharge model. A sinusoidal rf current density $J = \mathrm{Re}(J_0\, e^{j\omega t})$ flows through a discharge gap from $x = 0$ to $x = l$. The net heavy-particle positive charge density is assumed to be uniform and constant everywhere within the gap. An electron cloud of uniform density n_e and fixed width $d < l$ oscillates within the gap in response to the rf excitation, leading to the appearance of oscillating rf sheath regions near each electrode, with average sheath width $\bar{s} = \frac{1}{2}(l - d)$. The electric fields everywhere within the gap are calculated self-consistently from the homogeneous model, accounting for the plasma space charge effects. The homogeneous model sheath width $\bar{s} \approx J_0/(en\omega)$ is larger than a comparable sheath width found in experiments.[14] We therefore modify $\bar{s}$ by a factor $\eta < 1$. As discussed in Sec. IV, the value $\eta = 0.5$ is consistent with experimental results. The electron temperature T_e is assumed to be uniform in the bulk plasma and

a)Electronic mail: lieber@eecs.berkeley.edu.

oscillating in time at twice the rf. The electron power balance is solved analytically to determine the time-varying electron temperature, which also oscillates on the rf timescale. Averaging over the rf period yields effective rate coefficients for the gas phase activated processes. The particle balance relations for all species are then integrated numerically to determine the equilibrium discharge parameters. The coupling of analytical solutions of the time-varying discharge and electron temperature dynamics, and numerical solutions of the discharge chemistry, allows for a fast solution of the discharge equilibrium. The model is in one-dimensional planar geometry. To apply the model to the coaxial experimental configuration, we have unfolded the annular discharge region into a planar discharge with plate area $A = 11.5\,\pi \times 20$ mm^2 and a gap length $l = 1.5$ mm.

II. SPECIES, REACTIONS, AND RATE COEFFICIENTS

There are 32 simulation species used in the model: electrons e, Ar, Ar^m, Ar^r, Ar^{4p}, Ar^+, Ar_2^+, O_2, O_2^*, O_3, O, O^*, O_4^+, O_2^+, O^+, O^-, O_2^-, O_3^-, Cl_2, Cl, ClO, Cl^-, $TiCl_4$, $TiCl_3$, $TiOCl_2$, $TiOCl_3$, TiO_2, TiO_2Cl, TiO_2Cl_2, TiO_2Cl_3, $Ti_2O_2Cl_3$, and $Ti_2O_2Cl_4$. Ar^m includes the $^3P_2$ and $^3P_0$ metastable levels (reaction R11 in Table I), Ar^r, the $^1P_1$ and $^3P_1$ resonance levels (reaction R12 in Table I), and Ar^{4p}, all of the 4p levels. O_2^* is the $^1\Delta_g$ metastable, and O^* is the ^1D level. We do not include the Cl_2^+ and Cl^+ positive ions because the chlorine concentration is much smaller than the oxygen concentration, so the chlorine positive ion densities are expected to be much smaller than the oxygen ion densities. However, chlorine is highly attaching, so we include Cl^- in addition to the oxygen negative ions. For the titanium chemistry, we include the main expected neutral species.[11] We do not include titanium-containing negative ion species in the simulation. Such species can play a role in seeding the production of titanium-containing nanoparticles and in confining the titanium-containing species in the discharge as described below.

The argon, argon-oxygen, and oxygen-oxygen rate coefficients are given in Tables I–III. The argon-chlorine and oxygen-chlorine and chlorine-chlorine rate coefficients are given in Table IV. Reaction R1 for e-Ar elastic scattering gives the electron energy loss for this important process. The titanium species rate coefficients are given in Table V. We could not find any information in the literature on the electron- or metastable argon dissociation rate coefficients of $TiCl_4$ (reactions R175 and R176). For R175, we used the rate coefficient for the similar electron-$SiCl_4$ reaction,[16] but adjusted the activation energy to account for the difference in the dissociation energies of $TiCl_4$ and $SiCl_4$, and we assumed a threshold energy for $TiCl_4$ dissociation of 1.5 times the dissociation energy,[17] Similarly lacking any data, we used the attachment rate coefficient for O_3 (R43) for the Cl^- abstraction reactions R184–R186. For R176, we used the Ar^m quenching rate coefficient for the similar Ar^m-$SiCl_4$ and Ar^m-CCl_4 reactions,[18] and assumed that all quenching leads to dissociation.

Table VI gives the surface reactions, and the diffusion coefficients D and mobilities μ used in the model. At atmospheric pressure, the surface losses of the activated gas phase species Ar^m, Ar^r, Ar^{4p}, O^*, O_2^*, O, Cl, and ClO are limited by their diffusion rates to the surface, rather than the (much faster) reaction or recombination rates on the surface. We therefore assume that all these species are lost at diffusive rates, with a diffusion-limited loss flux to each wall $\Gamma = -D(\mathrm{d}n/\mathrm{d}x)_{\mathrm{wall}}$, which is evaluated for a parabolic density profile. The volume rate of loss of neutral species to the two walls is then $\mathrm{d}n/\mathrm{d}t = 12Dn/l^2$. The diffusion coefficients are calculated from gas kinetic theory[20] using the species Lennard-Jones parameters. For positive ions, a mobility-limited loss flux is assumed,[21,22] $\Gamma = \mu n_{+s}\bar{E}$, with n_{+s} the ion sheath density, $\bar{E}$ the time-average electric field at the wall, and with a unity reaction probability. This yields the volume rate of loss $\mathrm{d}n_+/\mathrm{d}t = 2\,\mu n_{+s}\bar{E}/l$. In this highly electronegative discharge, with $n_-/n_e \approx 40$, the total positive ion density in the sheath is n_e. For each ion species, we therefore use $n_{+s} = (n_+/n_{+,\mathrm{tot}})n_e$ in the calculations, with n_+ and $n_{+,\mathrm{tot}}$ the global ion and total ion densities, respectively. For the chlorinated titanium species, we assume no surface losses, due to the fluctuating conversion of these species to negative ions, such that, on the average, there is an electrostatic potential confining them in the discharge.[31] In principle, the same confinement occurs for the product molecule TiO_2, allowing the formation of nanoparticles within the discharge. There is some evidence that particulates form in the discharge: Nanoparticles have been observed to be deposited on the substrate after a deposition time of 1–2 min.[7] The buildup of higher mass chlorinated titanium species with negative charge through such reactions as

$$\mathrm{Ti}_{ix}\mathrm{O}_y\mathrm{Cl}_z^- + \mathrm{TiO_2Cl_3} \rightarrow \mathrm{Ti}_{ix+1}\mathrm{O}_{y'}\mathrm{Cl}_{z'}^- + (\mathrm{O, Cl\ products}) \tag{1}$$

can generate high mass species, which can follow the usual coagulation dynamics [Ref. 26, Sec. 17.4], leading to nanocrystal formation within the discharge. However, our model treats the discharge as a homogeneous gas phase mixture, so the formation of nanoparticles is beyond the scope of the present simulation. Therefore, we assume a diffusive loss of TiO_2 to the surface.

The deposition rate, DR, can be estimated from the total flux of TiO_2 depositing on the surface

$$\mathrm{DR} = \frac{\Gamma_{\mathrm{TiO_2}}}{n_f}, \tag{2}$$

where n_f is the film density. Due to the voids and exposed facets in the deposited films, we use a film density $n_f = 1.45 \times 10^{28}$ m^{-3} that is half of the TiO_2 solid density.

III. RESULTS

We consider an annular discharge with an outer radius $R_o = 6.5$ mm, an inner radius $R_i = 5$ mm, and a length $L = 2$ cm, similar to the experiment.[7] For the base case simulations, the total flow rate is taken to be 233 sccm with a $TiCl_4$ feed gas fraction $f_{\mathrm{TiCl_4}} = 7.3 \times 10^{-4}$, as these are the parameters of the base case experiment. The gas temperature at the

TABLE I. Electron impact reaction rate coefficients.

n	Reaction	Rate coefficient[a,b]	References
		Electron elastic scattering	
R1	$e + Ar \rightarrow e + Ar$	$2.34 \times 10^{-14} T_e^{1.61} e^{0.062(\log T_e)^2 - 0.117(\log T_e)^3}$	24
		Electron impact ionization	
R2	$e + Ar \rightarrow Ar^+ + e + e$	$2.3 \times 10^{-14} T_e^{0.59} e^{-17.44/T_e}$	24
R3	$e + Ar^m \rightarrow Ar^+ + e + e$	$6.8 \times 10^{-15} T_e^{0.67}$	24
R4	$e + Ar^{4p} \rightarrow Ar^+ + e + e$	$1.8 \times 10^{-13} T_e^{0.61} e^{-2.61/T_e}$	24
R5	$e + O \rightarrow O^+ + e + e$	$4.75 \times 10^{-15} T_e^{0.78} e^{-14.27/T_e}$	19
R6	$e + O^* \rightarrow O^+ + e + e$	$9.0 \times 10^{-15} T_e^{0.7} e^{-11.6/T_e}$	24
R7	$e + O_2 \rightarrow O_2^+ + e + e$	$2.01 \times 10^{-15} T_e^{1.09} e^{-12.41/T_e}$	19
R8	$e + O_2 \rightarrow O^+ + O + e + e$	$1.88 \times 10^{-16} T_e^{1.699} e^{-16.81/T_e}$	24
R9	$e + O_2^* \rightarrow O_2^+ + e + e$	$2.34 \times 10^{-15} T_e^{1.03} e^{-11.31/T_e}$	24
R10	$e + O_2^* \rightarrow O + O^+ + e + e$	$1.88 \times 10^{-16} T_e^{1.699} e^{-15.83/T_e}$	24
		Electron impact excitation and de-excitation	
R11	$e + Ar \rightarrow Ar^m + e$	$5 \times 10^{-15} e^{-12.64/T_e} + 1.4 \times 10^{-15} e^{-12.42/T_e}$	24, see text
R12	$e + Ar \rightarrow Ar^r + e$	$1.9 \times 10^{-15} e^{-12.6/T_e} + 2.7 \times 10^{-16} e^{-12.14/T_e}$	24, see text
R13	$e + Ar \rightarrow Ar^{4p} + e$	$2.16 \times 10^{-14} e^{-13.13/T_e}$	24
R14	$e + Ar^m \rightarrow Ar + e$	$4.3 \times 10^{-16} T_e^{0.74}$	24
R15	$e + Ar^m \rightarrow Ar^r + e$	3.7×10^{-13}	24
R16	$e + Ar^m \rightarrow Ar^{4p} + e$	$8.9 \times 10^{-13} T_e^{0.51} e^{-1.59/T_e}$	24
R17	$e + Ar^r \rightarrow Ar + e$	$4.3 \times 10^{-16} T_e^{0.74}$	24
R18	$e + Ar^r \rightarrow Ar^m + e$	9.106×10^{-13}	24
R19	$e + Ar^r \rightarrow Ar^{4p} + e$	$8.9 \times 10^{-13} T_e^{0.51} e^{-1.59/T_e}$	24
R20	$e + Ar^{4p} \rightarrow Ar^r + e$	$3 \times 10^{-13} T_e^{0.51}$	24
R21	$e + Ar^{4p} \rightarrow Ar^m + e$	$3 \times 10^{-13} T_e^{0.51}$	24
R22	$e + Ar^{4p} \rightarrow Ar + e$	$3.9 \times 10^{-16} T_e^{0.71}$	24
R23	$e + Ar^+ \rightarrow Ar^m$	$5.95 \times 10^{-17} T_e^{-0.5}$	22, He → Ar
R24	$e + e + Ar^+ \rightarrow e + Ar^m$	$5.6 \times 10^{-39} T_e^{-4.5}$	25
R25	$e + Ar_2^+ \rightarrow Ar^m + Ar$	$7.45 \times 10^{-14} T_e^{-0.67}$	25
R26	$e + O \rightarrow O^* + e$	$2.19 \times 10^{-14} T_e^{0.57} e^{-4.1/T_e}$	19
R27	$e + O^* \rightarrow O + e$	$8.17 \times 10^{-15} e^{-0.4/T_e}$	24
R28	$e + O^- \rightarrow O + e + e$	$4.64 \times 10^{-14} T_e^{0.5} e^{-3.44/T_e}$	19
R29	$e + O^+ \rightarrow O^*$	$4.66 \times 10^{-17} T_e^{-0.5}$	22
R30	$e + e + O^+ \rightarrow O^* + e$	$1.628 \times 10^{-21} T_e^{-4.5}$	22
R31	$e + O_2 \rightarrow O + O + e$	$9.49 \times 10^{-16} T_e^{0.38} e^{-11.84/T_e}$	19
R32	$e + O_2 \rightarrow O^* + O + e$	$8.45 \times 10^{-15} T_e^{0.38} e^{-11.84/T_e}$	19
R33	$e + O_2 \rightarrow O_2^* + e$	$1.25 \times 10^{-14} T_e^{-0.97} e^{-5.51/T_e}$	19
R34	$e + O_2^* \rightarrow O_2 + e$	$2.06 \times 10^{-15} e^{-1.163/T_e}$	24
R35	$e + O_2^* \rightarrow O + O + e$	$1.41 \times 10^{-15} T_e^{0.22} e^{-11.64/T_e}$	24
R36	$e + O_2^* \rightarrow O^* + O + e$	$1.29 \times 10^{-14} T_e^{0.22} e^{-11.64/T_e}$	24
R37	$e + O_2^* \rightarrow O^* + O^* + e$	$1.95 \times 10^{-16} T_e^{0.22} e^{-11.64/T_e}$	O_2 w. thresh. reduced
R38	$e + O_3 \rightarrow O + O_2 + e$	$1.42 \times 10^{-14} T_e^{-0.68} e^{-2.6/T_e}$	19
		Electron impact attachment and dissociative attachment	
R39	$e + O_2 \rightarrow O^- + O$	$1.12 \times 10^{-15} T_e^{-1.41} e^{-6.16/T_e}$	19
R40	$e + O_2 + O_2 \rightarrow O_2 + O_2^-$	$2.26 \times 10^{-42} (300/T_g)^{0.5}$	22
R41	$e + O_2^* \rightarrow O^* + O^-$	$9.93 \times 10^{-15} T_e^{-1.44} e^{-7.44/T_e}$	22
R42	$e + O_2^* \rightarrow O + O^-$	$4.33 \times 10^{-15} T_e^{-1.39} e^{-5.17/T_e}$	19
R43	$e + O_3 \rightarrow O^- + O_2$	$3.24 \times 10^{-15} T_e^{-0.94} e^{-0.91/T_e}$	19
R44	$e + O_3 \rightarrow O + O_2^-$	$9.56 \times 10^{-16} T_e^{-1.26} e^{-0.95/T_e}$	19
R45	$e + O_2 + Ar \rightarrow Ar + O_2^-$	$8.8 \times 10^{-42} T_e^{-0.5}$	22, He → Ar
		Dissociative recombination	
R46	$e + O_2^+ \rightarrow O + O$	$5.89 \times 10^{-14} T_e^{-1.06} e^{-0.51/T_e}$	27
R47	$e + O_2^+ \rightarrow O^* + O$	$4.688 \times 10^{-12} T_e^{-0.7}$	22
R48	$e + O_4^+ + \rightarrow O_2 + O_2$	$2.25 \times 10^{-13} T_e^{-0.5}$	30
R49	$e + e + O_4^+ \rightarrow O_2 + O_2 + e$	$7.18 \times 10^{-39} T_e^{-4.5}$	30

[a]Rate coefficients for 1, 2, and 3 reactants in s^{-1}, m^3/s, and m^6/s, respectively.
[b]Temperatures in roman and italic typeface in volts and Kelvins, respectively.

TABLE II. Electron impact reaction rate coefficients (cont'd).

n	Reaction	Rate coefficient[a,b]	References
	Ion–molecule reactions: Collisional detachment		
R50	$O^- + O \rightarrow O_2 + e$	$2 \times 10^{-16}(300/T_g)^{-0.5}$	22
R51	$O^- + O_2 \rightarrow O_3 + e$	$5 \times 10^{-18}(300/T_g)^{-0.5}$	22
R52	$O^- + O_2^* \rightarrow O_3 + e$	$3 \times 10^{-16}(300/T_g)^{0.5}$	22
R53	$O^- + O_3 \rightarrow O_2 + O_2 + e$	$3.02 \times 10^{-16}(300/T_g)^{-0.5}$	22
R54	$O_2^- + O \rightarrow O_3 + e$	$1.5 \times 10^{-16}(300/T_g)^{-0.5}$	22
R55	$O_2^- + O_2^* \rightarrow O_2 + O_2 + e$	$2 \times 10^{-16}(300/T_g)$	22
	Ion-molecule reactions: Argon ions		
R56	$Ar^+ + Ar + Ar \rightarrow Ar_2^+ + Ar$	2.7×10^{-43}	25
R57	$Ar^+ + O \rightarrow O^+ + Ar$	6.4×10^{-18}	24
R58	$Ar^+ + O^* \rightarrow O^+ + Ar$	6.4×10^{-18}	Use $Ar^+ + O$
R59	$Ar^+ + O_2 \rightarrow O_2^+ + Ar$	$4.9 \times 10^{-17}(300/T_g)^{0.78}$	24
R60	$Ar^+ + O^- \rightarrow O + Ar$	$4 \times 10^{-14}(300/T_g)^{0.43}$	24
	Ion-molecule reactions: Oxygen ions		
R61	$O^+ + O + O_2 \rightarrow O_2^+ + O_2$	$1.06 \times 10^{-42}(300/T_g)^{-0.5}$	22
R62	$O^+ + O + Ar \rightarrow O_2^+ + Ar$	$1.06 \times 10^{-41}(300/T_g)^{-0.5}$	22, He → Ar
R63	$O^+ + O_2 \rightarrow O_2^+ + O$	$2 \times 10^{-17}(300/T_g)^{0.4}$	22
R64	$O^+ + O_3 \rightarrow O_2^+ + O_2$	1.06×10^{-16}	22
R65	$O_2^+ + O_2 + O_2 \rightarrow O_4^+ + O_2$	$2.4 \times 10^{-42}(300/T_g)^{3.2}$	30
R66	$O_2^+ + O_2 + Ar \rightarrow O_4^+ + Ar$	$5.8 \times 10^{-43}(300/T_g)^{3.1}$	30
R67	$O_4^+ + Ar^m \rightarrow O + O + O_2 + Ar$	1.0×10^{-16}	30, He → Ar^m
R68	$O_4^+ + O \rightarrow O_2^+ + O_3$	3.0×10^{-16}	30
R69	$O_4^+ + O^* \rightarrow O_2^+ + O_3$	3.0×10^{-16}	30
R70	$O_4^+ + O_2 \rightarrow O_2^+ + O_2 + O_2$	$3.3 \times 10^{-12}(300T_g)^4 e^{-5030/T_g}$	30
R71	$O_4^+ + O_2^* \rightarrow O_2^+ + O_2 + O_2$	1.0×10^{-16}	30
R72	$O_4^+ + Ar \rightarrow O_2^+ + O_2 + Ar$	3.0×10^{-23}	30, He →Ar
R73	$O_2^* + O^- \rightarrow O_2^- + O$	1.06×10^{-16}	22
R74	$O^- + O_3 \rightarrow O_3^- + O$	$1.99 \times 10^{-16}(300/T_g)^{-0.5}$	22
R75	$O^- + O_3 \rightarrow O_2^- + O_2$	$1.02 \times 10^{-17}(300/T_g)^{-0.5}$	22
R76	$O_2^- + O \rightarrow O_2 + O^-$	$1.5 \times 10^{-16}(300/T_g)^{-0.5}$	22
R77	$O_2^- + O_3 \rightarrow O_2 + O_3^-$	$6 \times 10^{-16}(300/T_g)$	22
R78	$O_3^- + O \rightarrow O_2^- + O_2$	$2.5 \times 10^{-16}(300/T_g)^{-0.5}$	22
	Ion-ion recombination		
R79	$O^+ + O^- + Ar \rightarrow O + O + Ar$	$2 \times 10^{-37}(300/T_g)^{2.5}$	22, He → Ar
R80	$O^- + O^+ \rightarrow O + O$	$2 \times 10^{-13}(300/T_g)$	22
R81	$O^- + O^+ + O_2 \rightarrow O + O + O_2$	$2 \times 10^{-37}(300/T_g)^{2.5}$	22
R82	$O^- + Ar^+ + Ar \rightarrow Ar + Ar + O$	$2 \times 10^{-37}(300/T_g)^{2.5}$	22, He → Ar
R83	$O^- + O_2^+ \rightarrow O + O_2$	$2 \times 10^{-13}(300/T_g)$	22
R84	$O^- + O_2^+ \rightarrow O + O + O$	1.02×10^{-13}	22
R85	$O^- + O_2^+ + O_2 \rightarrow O + O_2 + O_2$	$2 \times 10^{-37}(300/T_g)^{2.5}$	22
R86	$O^- + O_2^+ + Ar \rightarrow O + O_2 + Ar$	$2 \times 10^{-37}(300/T_g)^{2.5}$	22, He → Ar
R87	$O^- + O_2^+ + O_2 \rightarrow O_2 + O_3$	$2 \times 10^{-37}(300/T_g)^{2.5}$	22
R88	$O_2^- + O_2^+ \rightarrow O_2 + O_2$	$2 \times 10^{-13}(300/T_g)$	22
R89	$O_2^- + O_2^+ \rightarrow O_2 + O + O$	1.06×10^{-13}	22
R90	$O_2^- + O^+ \rightarrow O_2 + O$	$2 \times 10^{-13}(300/T_g)$	22
R91	$O_3^- + O_2^+ \rightarrow O_3 + O_2$	$2 \times 10^{-13}(300/T_g)$	22
R92	$O_3^- + O_2^+ \rightarrow O_3 + O + O$	2×10^{-13}	22
R93	$O_3^- + O^+ \rightarrow O_3 + O$	$2 \times 10^{-13}(300/T_g)$	22
R94	$O_4^+ + O^- \rightarrow O_2 + O_2 + O$	1.0×10^{-13}	30
R95	$O_4^+ + O_2^- \rightarrow O_2 + O_2 + O_2$	1.0×10^{-13}	30
R96	$O_4^+ + O_3^- \rightarrow O_2 + O_2 + O_2 + O$	1.0×10^{-13}	30
R97	$O_4^+ + O^- + Ar \rightarrow O_2 + O_2 + O + Ar$	$2.0 \times 10^{-37}(300/T_g)^{2.5}$	30
R98	$O_4^+ + O_2^- + Ar \rightarrow O_2 + O_2 + O_2 + Ar$	$2.0 \times 10^{-37}(300/T_g)^{2.5}$	30
R99	$O_4^+ + O_3^- + Ar \rightarrow O_2 + O_2 + O_3 + Ar$	$2.0 \times 10^{-37}(300/T_g)^{2.5}$	30

[a]Rate coefficients for 1, 2, and 3 reactants in s^{-1}, m^3/s, and m^6/s, respectively.
[b]Temperatures in roman and italic typeface in volts and Kelvins, respectively.

TABLE III. Neutral reaction rate coefficients.

n	Reaction	Rate coefficient[a,b]	References
	Neutral reactions: Penning ionization		
R100	$Ar^m + Ar^r \rightarrow Ar + Ar^+ + e$	2.106×10^{-15}	24
R101	$Ar^{4p} + Ar^{4p} \rightarrow Ar + Ar^+ + e$	5×10^{-16}	24
R102	$Ar^m + Ar^m \rightarrow Ar + Ar^+ + e$	6.4×10^{-16}	24
	Neutral reactions: Argon atom		
R103	$Ar + Ar^m \rightarrow Ar + Ar$	2.106×10^{-21}	24
R104	$Ar^m + O_2 \rightarrow O + O + Ar$	1.01×10^{-16}	24
R105	$Ar^m + O_2 \rightarrow O + O^* + Ar$	1.14×10^{-16}	24
R106	$Ar^m + O \rightarrow O + Ar$	4.10×10^{-17}	24
R107	$O_2 + Ar^{4p} \rightarrow O + O + Ar$	2.96×10^{-16}	24
R108	$O_2 + Ar^{4p} \rightarrow O + O^* + Ar$	3.34×10^{-16}	24
R109	$O^* + Ar \rightarrow O + Ar$	3×10^{-19}	24
R110	$O_2^* + Ar \rightarrow O_2 + Ar$	$3 \times 10^{-24} e^{-200/T_g}$	Use $O_2^* + O_2$
R111	$O + O + Ar \rightarrow O_2 + Ar$	1.06×10^{-45}	22, He → Ar
R112	$O + O + Ar \rightarrow O_2^* + Ar$	$9.88 \times 10^{-47} (300/T_g)$	22, He → Ar
R113	$O + O_2 + Ar \rightarrow O_3 + Ar$	$3.4 \times 10^{-46} (300/T_g)^{1.2}$	22, He → Ar
	Neutral reactions: Oxygen atom		
R114	$O_3 + O \rightarrow O + O + O_2$	$1.56 \times 10^{-15} e^{-11490/T_g}$	22
R115	$O + O_3 \rightarrow O_2 + O_2$	$1.5 \times 10^{-17} e^{-2250/T_g}$	22
R116	$O_3 + O_2 \rightarrow O_2 + O_2 + O$	$1.56 \times 10^{-15} e^{-11490/T_g}$	22
R117	$O_3 + O_3 \rightarrow O_2 + O + O_3$	$1.56 \times 10^{-15} e^{-11490/T_g}$	22
R118	$O_2 + O^* \rightarrow O + O_2^*$	1.0×10^{-18}	22
R119	$O + O^* \rightarrow O + O$	8×10^{-18}	22
R120	$O^* + O_2 \rightarrow O + O_2^*$	$1.6 \times 10^{-18} e^{-67/T_g}$	22
R121	$O^* + O_2 \rightarrow O + O_2$	$4.8 \times 10^{-18} e^{-67/T_g}$	22
R122	$O^* + O_3 \rightarrow O_2 + O + O$	1.2×10^{-16}	22
R123	$O^* + O_3 \rightarrow O_2 + O_2$	1.2×10^{-16}	22
R124	$O_2^* + O_2 \rightarrow O_2 + O_2$	$3 \times 10^{-24} e^{-200/T_g}$	22
R125	$O_2^* + O_2 \rightarrow O + O_3$	$2.95 \times 10^{-27} (300/T_g)^{0.5}$	22
R126	$O_2^* + O_3 \rightarrow O_2 + O_2 + O$	$5.2 \times 10^{-17} e^{-2840/T_g}$	22
R127	$O_2^* + O_2^* \rightarrow O_2 + O_2$	$9 \times 10^{-23} e^{-560/T_g}$	22
R128	$O_2^* + O \rightarrow O_2 + O$	2×10^{-22}	22
R129	$O_2^* + O_3 \rightarrow O_2 + O_2 + O^*$	1.01×10^{-17}	22
R130	$O + O + O \rightarrow O_2 + O$	$9.22 \times 10^{-46} (300/T_g)$	22
R131	$O + O + O \rightarrow O_2^* + O$	$6.93 \times 10^{-47} (300/T_g)$	22
R132	$O + O + O_2 \rightarrow O_2 + O_2$	$2.56 \times 10^{-46} (300/T_g)$	22
R133	$O + O + O_2 \rightarrow O_2^* + O_2$	$1.93 \times 10^{-47} (300/T_g)$	22
R134	$O + O + O_2 \rightarrow O_3 + O$	$3.4 \times 10^{-46} (300/T_g)^{1.2}$	22
R135	$O + O_2 + O_2 \rightarrow O_3 + O_2$	$6 \times 10^{-46} (300/T_g)^{2.8}$	22
R136	$O_2 + O + O_2^* \rightarrow O_2 + O_2 + O$	1.00×10^{-44}	22
R137	$O_3 + O + O_2 \rightarrow O_3 + O_3$	$2.27 \times 10^{-47} e^{1057/T_g}$	22
	Radiation		
R138	$Ar^r \rightarrow Ar$	1.1×10^5	24
R139	$Ar^{4p} \rightarrow Ar^m$	3×107	24
R140	$Ar^{4p} \rightarrow Ar^r$	3×10^7	24

[a]Rate coefficients for 1, 2, and 3 reactants in s^{-1}, m^3/s, and m^6/s, respectively.
[b]Temperatures in roman and italic typeface in volts and Kelvins, respectively.

inlet is $T_i = 300$ K, and measurements using OH rotational spectroscopy indicate a gas temperature in the discharge of $T_g = 625$ K, which is used in the simulations. Because the inner and outer coaxial copper electrodes have relatively uniform temperatures along their lengths, and the thermal conduction time of the gas is much shorter than the flow time of the gas through the system, we assume an isothermal flow. The flow is laminer because of the small flow velocity. The required discharge power P is estimated from the gas heating and the external convection and radiation losses of the reactor to the ambient environment

$$P = \frac{3}{2} n_{gi} k (T_g - T_i) u_i \, 2\pi R l + h_{c+r} (T_g - T_i) 2\pi R L, \quad (3)$$

where n_{gi} is the gas density at the inlet, k is Boltzmann's constant, u_i is the flow velocity, R is the mean radius, $h_{c+r} \approx 34$ W/m^2 K

TABLE IV. Chlorine rate coefficients.

n	Reaction	Rate coefficient[a,b]	References
R141	$e + Cl_2 \rightarrow Cl + Cl + e$	$1.04 \times 10^{-13} T_e^{-0.29} e^{-8.84/T_e}$ $3.43 \times 10^{-15} T_e^{1.18} e^{-3.98/T_e}$	28
R142	$e + Cl_2 \rightarrow Cl + Cl^-$	$+3.05 \times 10^{-16} T_e^{-1.33} e^{-0.11/(T_e+0.014)}$	28
R143	$e + Cl^- \rightarrow Cl + e + e$	$9.02 \times 10^{-15} T_e^{0.92} e^{-4.88/T_e}$	28
R144	$Cl + Cl + Cl_2 \rightarrow Cl_2 + Cl_2$	$3.5 \times 10^{-45} e^{810/T_g}$	28
R145	$Cl + Cl + Cl \rightarrow Cl_2 + Cl$	$8.75 \times 10^{-46} e^{810/T_g}$	28
R146	$Cl^- + Ar^+ \rightarrow Cl + Ar$	$5 \times 10^{-14} (300/T_g)^{0.5}$	28
R147	$Cl + Cl + Ar \rightarrow Cl_2 + Ar$	$8.75 \times 10^{-46} e^{-810/T_g}$	28
R148	$Cl + Cl + Ar^m \rightarrow Cl_2 + Ar$	$8.75 \times 10^{-46} e^{-810/T_g}$	28
R149	$Ar_2^+ + Cl^- \rightarrow Ar + Ar + Cl$	$5 \times 10^{-14} (300/T_g)^{0.5}$	28
R150	$Cl^- + O_2^+ \rightarrow Cl + O_2$	$5 \times 10^{-14} (300/T_g)^{0.5}$	19
R151	$Cl^- + O^+ \rightarrow Cl + O$	$5 \times 10^{-14} (300/T_g)^{0.5}$	19
R152	$Cl_2 + O_2^* \rightarrow Cl_2 + O_2$	$2.2 \times 10^{-24} (300/T_g)^{-0.8}$	19
R153	$Cl_2 + O^* \rightarrow Cl_2 + O$	$7 \times {}^{-17}$	19
R154	$Cl + O_2^* \rightarrow Cl + O_2$	1.3×10^{-22}	19
R155	$Cl + O^* \rightarrow Cl + O$	8×10^{-18}	19
R156	$e + ClO \rightarrow Cl + O + e$	$1.27 \times 10^{-13} T_e^{-1.36} e^{-6.84/T_e}$	19
R157	$O^* + ClO \rightarrow Cl + O_2$	$4.11 \times 10^{-17} e^{42/T_g}$	19
R158	$O + ClO \rightarrow Cl + O_2$	$4.11 \times 10^{-17} e^{42/T_g}$	19
R159	$Cl_2 + O \rightarrow Cl + ClO$	$7.4 \times 10^{-18} e^{-1650/T_g}$	19
R160	$Cl_2 + O^* \rightarrow Cl + ClO$	2.11×10^{-16}	19
R161	$Cl + O_3 \rightarrow O_2 + ClO$	$2.49 \times 10^{-17} e^{-233/T_g}$	19
R162	$ClO + ClO \rightarrow Cl_2 + O_2$	6.38×10^{-21}	19
R163	$ClO + ClO \rightarrow Cl_2 + O + O$	1.56×10^{-20}	19

[a]Rate coefficients for 1, 2, and 3 reactants in s^{-1}, m^3/s, and m^6/s, respectively.
[b]Temperatures in roman and italic typeface in volts and Kelvins, respectively.

TABLE V. Titanium rate coefficients.

n	Reaction	Rate coefficient[a,b]	References
R164	$TiCl_3 + Cl_2 \rightarrow TiCl_4 + Cl$	1.6×10^{-17}	11
R165	$TiCl_3 + ClO \rightarrow TiCl_4 + O$	1.6×10^{-17}	11
R166	$TiCl_4 + Ti_2O_2Cl_3 \rightarrow TiCl_3 + Ti_2O_2Cl_4$	1.6×10^{-17}	11
R167	$TiCl_3 + O_2 \rightarrow TiO_2Cl_3$	1.6×10^{-17}	11
R168	$TiCl_3 + TiO_2Cl_3 \rightarrow TiOCl_3 + TiOCl_3$	1.6×10^{-17}	11
R169	$TiOCl_3 + O \rightarrow TiCl_3 + O_2$	1.6×10^{-17}	11
R170	$TiOCl_3 + ClO \rightarrow TiO_2Cl_3 + Cl$	1.6×10^{-17}	11
R171	$TiOCl_3 + O \rightarrow TiO_2Cl_3$	1.6×10^{-17}	11
R172	$TiOCl_2 + Cl \rightarrow TiOCl_3$	1.6×10^{-17}	11
R173	$TiOCl_3 + TiOCl_2 \rightarrow Ti_2O_2Cl_4 + Cl$	1.6×10^{-17}	11
R174	$TiOCl_2 + TiOCl_2 \rightarrow Ti_2O_2Cl_4$	1.6×10^{-17}	11
R175	$e + TiCl_4 \rightarrow e + TiCl_3 + Cl$	$7.27 \times 10^{-15} T_e^{0.5} e^{-5.37/T_e}$	See text
R176	$Ar^m + TiCl_4 \rightarrow TiCl_3 + Cl + Ar$	$3.1 \times 10^{-15} T_g^{0.5}$	See text
R177	$TiCl_4 + O \rightarrow TiCl_3 + ClO$	$5.36 \times 10^{-16} e^{-14200/T_g}$	11
R178	$TiCl_3 + Ti_2O_2Cl_4 \rightarrow TiCl_4 + Ti_2O_2Cl_3$	$3.37 \times 10^{-16} e^{-3490/T_g}$	11
R179	$TiOCl_3 + TiOCl_3 \rightarrow TiCl_3 + TiO_2Cl_3$	$1.837 \times 10^{-19} e^{-842/T_g}$	11
R180	$TiCl_3 + O_2 \rightarrow TiOCl_3 + O$	$1.4 \times 10^{-16} e^{-13000/T_g}$	11
R181	$TiO_2Cl_3 + Cl \rightarrow TiOCl_3 + ClO$	$1.28 \times 10^{-15} e^{-13840/T_g}$	11
R182	$TiCl_3 + O \rightarrow TiOCl_2 + Cl$	1.6×10^{-17}	11
R183	$TiOCl_3 \rightarrow TiOCl_2 + Cl$	$3.37 \times 10^{-11} n_{Ar} e^{-19490/T_g}$	11
R184	$e + TiO_2Cl_3 \rightarrow TiO_2Cl_2 + Cl^-$	$3.24 \times 10^{-15} T_e^{-0.94} e^{-0.91/T_e}$	See text
R185	$e + TiO_2Cl_2 \rightarrow TiO_2Cl + Cl^-$	$3.24 \times 10^{-15} T_e^{-0.94} e^{-0.91/T_e}$	See text
R186	$e + TiO_2Cl \rightarrow TiO_2 + Cl^-$	$3.24 \times 10^{-15} T_e^{-0.94} e^{-0.91/T_e}$	See text

[a]Rate coefficients for 1, 2, and 3 reactants in s^{-1}, m^3/s, and m^6/s, respectively.
[b]Temperatures in roman and italic typeface in volts and Kelvins, respectively.

TABLE VI. Surface reactions, diffusion coefficients D, and mobilities μ.

n	Reaction	D (m^2/s)	μ (m^2/V s)	References
R187	$O_2^+ \rightarrow O_2$	…	5.6×10^{-4}	29
R188	$Ar^m \rightarrow Ar$	1.09×10^{-5}	…	29
R189	$Ar^+ \rightarrow Ar$	…	3.0×10^{-4}	29
R190	$Ar_2^+ \rightarrow Ar + Ar$	…	3.9×10^{-4}	29
R191	$O^+ \rightarrow \frac{1}{2}O_2$	…	7.0×10^{-4}	29
R192	$Ar^r \rightarrow Ar$	1.09×10^{-5}	…	Same as Ar^m
R193	$Ar^{4p} \rightarrow Ar$	1.09×10^{-5}	…	Same as Ar^m
R194	$O^* \rightarrow O$	9.41×10^{-5}	…	Lennard-Jones[19]
R195	$O^* \rightarrow \frac{1}{2}O_2$	9.41×10^{-5}	…	Lennard-Jones[19]
R196	$O_2^* \rightarrow O_2$	6.07×10^{-5}	…	Lennard-Jones[19]
R197	$O \rightarrow \frac{1}{2}O_2$	9.41×10^{-5}	…	Lennard-Jones[19]
R198	$O_4^+ \rightarrow O_2 + O_2$	…	4.0×10^{-4}	Lennard-Jones[19]
R199	$Cl \rightarrow \frac{1}{2}Cl_2$	5.99×10^{-5}	…	Lennard-Jones[19]
R200	$Cl \rightarrow ClO$	5.99×10^{-5}	…	Lennard-Jones[19]
R201	$TiO_2 \rightarrow$ wall	4.0×10^{-5}	…	Lennard-Jones

is the heat transfer coefficient,[23] and $l = R_o - R_i = 1.5$ mm is the discharge gap width. Equation (3) yields $P = 8.6$ W (1.2 W/cm^2 of plate area), which we use in the simulations. One should note that the power applied to the discharge in the experiment is on the order of 100 W, which is much higher than the power of 8.6 W dissipated in the discharge as determined from Eq. (3). This is probably due to high external losses in the matching network and external circuit, and is a feature commonly seen in atmospheric pressure rf plasma discharges [Ref. 21, p. 76]. As will be shown, a power of 8.6 W yields a current density of 370 A/m^2 for the standard case in the simulation, which is consistent with previously published experimental data.[14] We discuss this further in our conclusions in Sec. IV.

The simulations are done using the Matlab stiff integrator ode15s and are started with low densities of all dissociated and charged species, and the simulation time is $t_f = 0.13$ s, corresponding to the time for the feed gas to flow from the inlet to the outlet of the system. A typical simulation takes less than 2 min on a medium-speed laptop computer. As a check on the integration accuracy, we determined the electron density by two methods: (1) by direct integration of the electron balance equation; (2) by summing the heavy particle charge densities. The two methods agree to within 1% for all results presented in this work.

In the next four figures, we show the variations of the discharge parameters with the oxygen feed gas fraction f_{O_2}. A minimum $f_{O_2} \approx 7.3 \times 10^{-4}$ is required; below this value there is not enough oxygen for pure TiO_2 deposition. Figures 1 and 2 give the neutral densities in the discharge. By far the most important neutral precursor for the film deposition is seen to be TiO_2Cl_3, with subsequent Cl abstraction by dissociative attachment to form the final product TiO_2. $TiCl_4$ is converted almost entirely into TiO_2Cl_3, except at the highest values of f_{O_2}. The simulations indicate that all species have equilibrated (generation rate ≈ loss rate) except for the feed gas $TiCl_4$ and the dimer $Ti_2O_2Cl_4$. For $TiCl_4$, the loss rate (dissociation of $TiCl_4$) remains much larger than the production rate at the final time t_f. For $Ti_2O_2Cl_4$, the loss rate

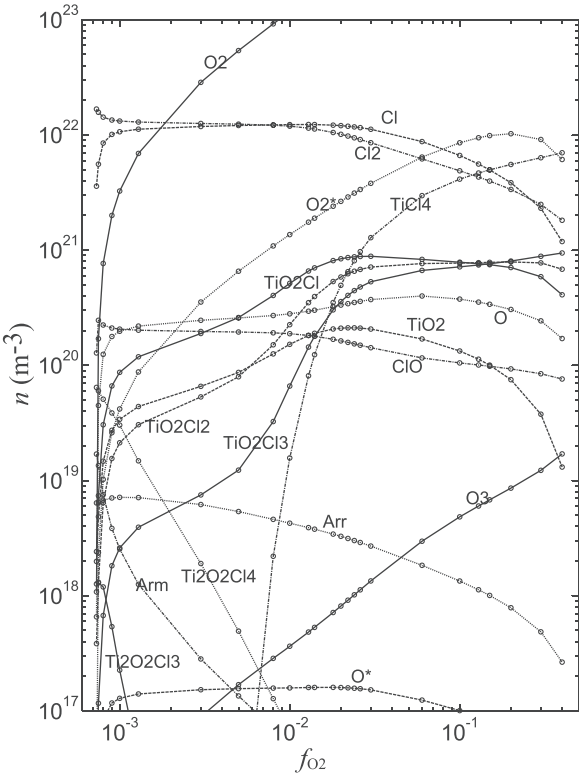

FIG. 1. Part I of neutral densities n versus O_2 fraction f_{O_2} at $t_f = 0.13$ s, for 233 sccm flow rate with gas temperature $T_g = 625$ K and $TiCl_4$ fraction $f_{TiCl_4} = 7.3 \times 10^{-4}$.

(reaction R178) is smaller than the generation. Figure 3 gives the densities of the charged species. The dominant positive and negative ions are found to be Ar_2^+ and Cl^-, except at the highest values of f_{O_2}, where O_2^+ is dominant. Over most of the range of f_{O_2}, the electronegativity (ratio of negative ion to electron density) is around 40. Figure 4 gives the TiO_2 deposition rate, which is seen to peak at about 2.35 nm/s when $f_{O_2} = 0.01$. The base case deposition rate is 1.25 nm/s. With increasing O_2 fraction, the deposition rate at 0.13 s first rises due to increased precursor formation and then falls as the TiO_2 density is itself depleted at the earlier times.

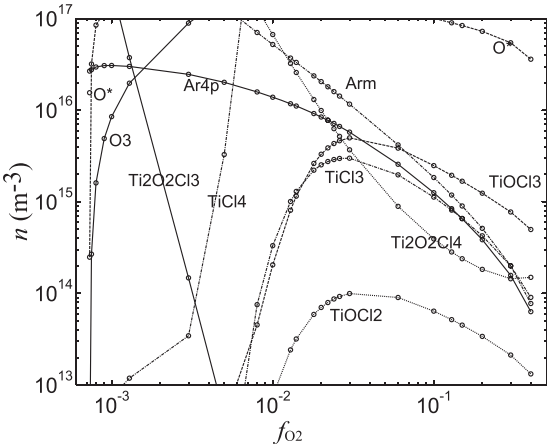

FIG. 2. Part II of neutral densities n versus O_2 fraction f_{O_2} at $t_f = 0.13$ s, for 233 sccm flow rate with gas temperature $T_g = 625$ K and $TiCl_4$ fraction $f_{TiCl_4} = 7.3 \times 10^{-4}$.

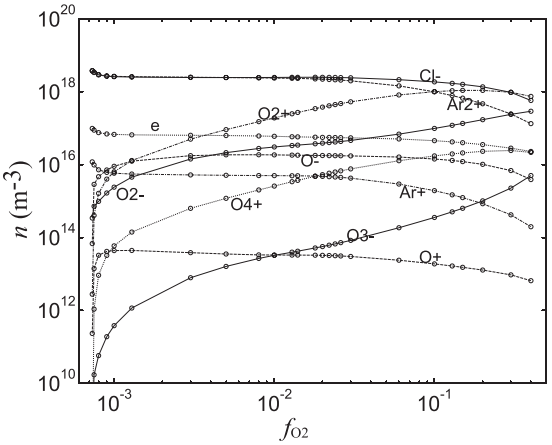

FIG. 3. Charged particle densities n versus O_2 fraction f_{O_2} at $t_f = 0.13$ s, for 233 sccm flow rate with gas temperature $T_g = 625$ K and $TiCl_4$ fraction $f_{TiCl_4} = 7.3 \times 10^{-4}$.

The simulation also yields the discharge rf voltage V_{rf}, as well as the rf bulk plasma voltage V_{bulk} and the rf sheath voltage V_{sheath}. For a power of 8.6 W, corresponding to an rf current of 370 A/m^2, V_{rf} varies from 300 V to 1100 V with the change of f_{O_2}. The current density is consistent with previous measurements of rf current at 13.56 MHz in a pure argon atmospheric pressure discharge.[14] The base case voltage of 631 V is smaller than the measured rf voltage across the discharge of about 1300 V, possibly due to additional voltage drops across the tube walls (≈210 V) and the driving circuit. The simulation shows that there is a resistive bulk voltage component of about 40–60 V, while the sheath voltages are capacitive. The electron temperature T_e in the discharge oscillates in time at twice the rf frequency, having an average value of 0.922 V and an oscillation amplitude of 0.915 V for the base case f_{O_2}. The sheath width $\bar{s}$ is about 0.32 mm for the base case.

Although the sheath voltages are large, ions crossing the sheath continuously lose energy by collisions with neutral gas atoms. At atmospheric pressure, these ions in the sheath typically have thermal energies, as the ion drift velocity is small compared to the ion thermal velocity. To see this, the

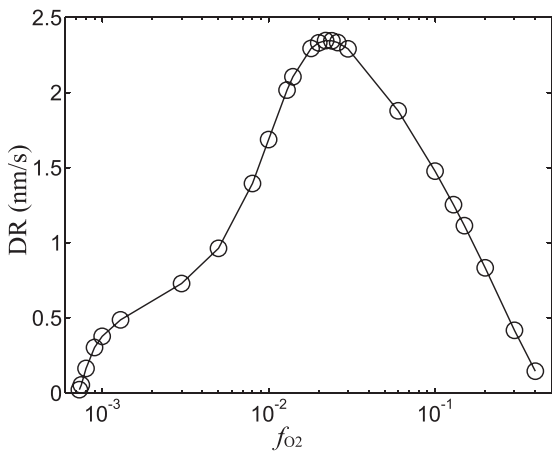

FIG. 4. TiO_2 film deposition rate versus O_2 fraction f_{O_2} at $t_f = 0.13$ s, for 233 sccm flow rate with gas temperature $T_g = 625$ K and $TiCl_4$ fraction $f_{TiCl_4} = 7.3 \times 10^{-4}$.

ion bombarding energy $\mathcal{E}_i$ can be estimated from the mean velocity of ions bombarding the wall, $v_i = \mu_+ \bar{E}$, as $\mathcal{E}_i = M_i v_i^2/2e$. For the dominant Ar_2^+ ions with the base case $f_{O_2} = 0.129$, we find $\bar{E} = 2.41 \times 10^5$ V/m from the simulation, and using the mobility in Table VI gives $v_i = 42.2$ m/s. This corresponds to an energy of $\mathcal{E}_i = 0.0008$ V, which is small compared to the thermal gas energy $\frac{3}{2}T_g = 0.08$ V. We conclude that ions near the wall have thermal energies and that ion bombardment of the substrate does not play a role in film formation.

Although the reaction set is complicated, the simulation results indicate that the precursor generation can be understood in terms of a series reaction chain with two reactive intermediate species: Ar^m and $TiCl_3$. At the base case $f_{O_2} = 0.129$, metastable argon is mainly generated by electron excitation of Ar (88% from reaction R11), and is mainly lost by dissociation of O_2 to form O and O^* (R104 and R105)

$$\frac{dn_{Ar^m}}{dt} = K_{11} n_e n_{Ar} - (K_{104} + K_{105}) n_{Ar^m} n_{O_2} \approx 0. \quad (4)$$

This yields

$$n_{Ar^m} = \frac{K_{11}}{K_{104} + K_{105}} \frac{n_{Ar}}{n_{O_2}} n_e. \quad (5)$$

We note that $n_{Ar^m} \propto n_e$. The feed gas $TiCl_4$ is lost by electron (81% from R175) and Penning (19% from R176) dissociation to form $TiCl_3$

$$\frac{dn_{TiCl_4}}{dt} = -\nu_L n_{TiCl_4}, \quad (6)$$

where $\nu_L = K_{175} n_e + K_{176} n_{Ar^m}$ is the first order rate coefficient for loss of $TiCl_4$. The solution of Eq. (6) is

$$n_{TiCl_4} = n_{TiCl_4}(0)\, e^{-\nu_L t}, \quad (7)$$

which shows exponential decay of the titanium feedstock from its initial density $n_{TiCl_4}(0)$. The reactive intermediate $TiCl_3$ is almost entirely formed by the above dissociations and is almost entirely lost by the reaction of $TiCl_3$ with O_2 (reaction R167) to form the precursor species TiO_2Cl_3

$$\frac{dn_{TiCl_3}}{dt} = \nu_L n_{TiCl_4} - K_{167} n_{TiCl_3} n_{O_2} \approx 0. \quad (8)$$

This yields

$$n_{TiCl_3} = \frac{\nu_L}{K_{167}} \frac{n_{TiCl_4}}{n_{O_2}}. \quad (9)$$

Finally, TiO_2Cl_3 is almost entirely generated by the preceding loss reaction and is lost by dissociative attachment to form TiO_2Cl_2 (reaction R184), subsequent dissociative attachment form TiO_2Cl from TiO_2Cl_2, and TiO_2 from TiO_2Cl (reactions R185 and R186, respectively),

$$\frac{dn_{TiO_2Cl_3}}{dt} = \nu_L n_{TiCl_4} - \nu n_{TiO_2Cl_3}, \quad (10)$$

$$\frac{dn_{TiO_2Cl_2}}{dt} = \nu n_{TiO_2Cl_3} - \nu n_{TiO_2Cl_2}, \quad (11)$$

$$\frac{dn_{TiO_2Cl}}{dt} = \nu n_{TiO_2Cl_2} - \nu n_{TiO_2Cl}, \quad (12)$$

$$\frac{dn_{TiO_2}}{dt} = \nu n_{TiO_2Cl} - \nu_W n_{TiO_2}, \quad (13)$$

where $\nu = K_{att} n_e$ is the dissociative attachment loss frequency, and $\nu_W = 12 D_{TiO_2}/l^2$ is the first order rate coefficient for loss to the walls.

Equations (6) and (10)–(13) can be solved by Laplace transformation, as described in the Appendix. The base case ($f_{O_2} = 0.129$) parameters are $\nu_L = 4.6$, $\nu = 31.7$, and $\nu_W = 213.3\,s^{-1}$. Figure 5 shows the deposition rate versus the time t from the simulation (solid line) and from the theory (dashed line) based on

$$DR = \frac{\Gamma_{TiO_2}}{n_f} = \frac{6 D_{TiO_2} n_{TiO_2}}{n_f l}. \quad (14)$$

The time when the TiO_2 density rises to a maximum value is

$$t_{max} \approx \frac{1}{\nu_L - \nu} \ln \frac{\nu_L}{\nu} + \frac{2}{\nu}, \quad (15)$$

which gives $t_{max} \approx 0.13\,s$ for the basic case. There is a reasonable agreement between the simulation and the theory, indicating that the precursor generation can be understood in terms of a series reaction chain with the reactive intermediate species Ar^m and $TiCl_3$.

Figure 6 shows the deposition rate DR versus total power S_{tot} as the solid line. This variation can be qualitatively understood in terms of the theory, as the electron density n_e scales roughly linearly with the power. Because ν_L and ν scale linearly with n_e, this implies a roughly linear scaling of ν_L and ν with the power per unit area S_{tot}. Setting the constant of proportionality from the base case yields $\nu_L = 3.8\,S_{tot}$ and $\nu = 26.4\,S_{tot}$. Using these in Eq. (14) and evaluating at $t = t_f$, we obtain the variation of n_{TiO_2} with S_{tot},

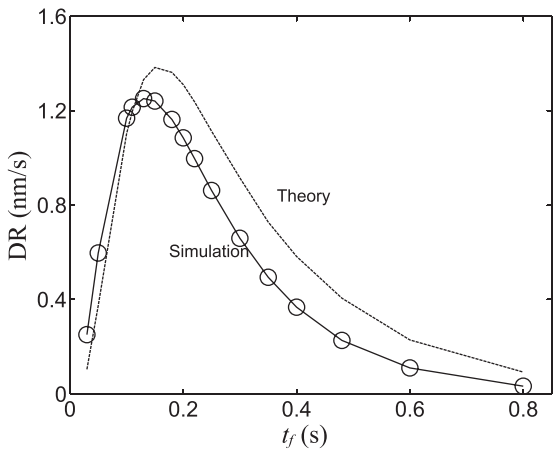

FIG. 5. TiO_2 film deposition rate versus integration time t_f, for 233 sccm flow rate with gas temperature $T_g = 625\,K$, O_2 fraction $f_{O_2} = 0.129$, and $TiCl_4$ fraction $f_{TiCl_4} = 7.3 \times 10^{-4}$.

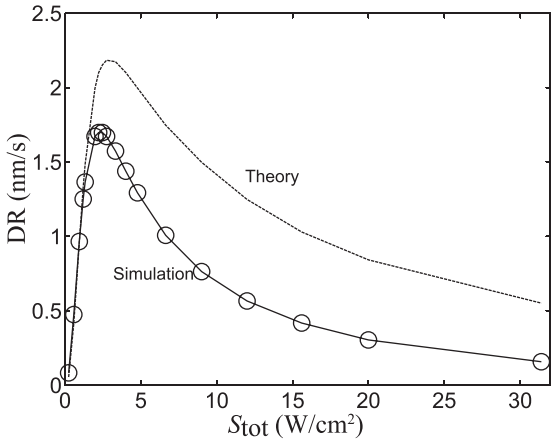

FIG. 6. TiO_2 film deposition rate versus total discharge power S_{tot} at $t_f = 0.13$ s, for 233 sccm total flow rate with gas temperature $T_g = 625\,K$, O_2 fraction $f_{O_2} = 0.129$, and $TiCl_4$ fraction $f_{TiCl_4} = 7.3 \times 10^{-4}$.

from which we can evaluate the deposition rate. The result is shown as the dashed line in the figure. Except for the somewhat higher maximum in the theoretical deposition rate, the simulation and theory agree quite well. For the readers' reference, the percentages of the main reactions in the full model that are used in the simplified scheme are given in Table VII.

IV. CONCLUSIONS AND FURTHER DISCUSSION

We have used a hybrid global-analytical model of an atmospheric pressure rf driven capacitive discharge in $Ar/O_2/TiCl_4$ feed gas mixture to determine the plasma conditions for TiO_2 film deposition. The base case feed gas mixture was $Ar/O_2/TiCl_4$ with flow rates of 203/30/0.17 sccm, and with a gas temperature of 625 K. Variations of the discharge parameters and species densities with O_2 concentration and discharge power were determined. The results indicate that the active precursor species is TiO_2Cl_3, with subsequent chlorine atom abstraction by dissociative attachment. The expected deposition rates are around 1 nm/s, which are consistent with measured deposition rates.[7] The simulation results indicate that the deposition rate is strongly affected by the oxygen fraction f_{O_2} and theoretically, the maximum expected deposition rate is several nm/s. The discharge rf voltage and current amplitudes depend only weakly on f_{O_2}.

The sheath width reduction factor $\eta = 0.5$ that we used in our simulations is consistent with previously published

TABLE VII. Percentages of the main reactions in the full model used in the simplified chemical scheme; 100% is used in the simplified scheme; the creation and loss of TiO_2Cl_2, TiO_2Cl, and TiO_2 is 100% for both the full model and the simplified scheme.

Process	Reactions	Full simulation (%)
Ar^m creation	R11	88
Ar^m loss	R104 + R105	99
$TiCl_4$ loss	R175 + R176	100
$TiCl_3$ creation	R175 + R176	100
$TiCl_3$ loss	R167	100
TiO_2Cl_3 creation	R167	100
TiO_2Cl_3 loss	R184	100

data on rf-excited atmospheric pressure argon discharges.[14] In an experiment with a 1.6 mm gap, the discharge could be maintained in a transversely homogeneous "α-mode" only at rf frequencies above about 6 MHz. The authors state that this frequency limit is set by the oscillation amplitude of the electrons, i.e., the sheath width. This result is consistent with the scaling of the average rf sheath width $\bar{s}$ with frequency for the homogeneous model[32]

$$\omega\bar{s} = (6\zeta e T_e/M_{\mathrm{He}})^{1/2}, \tag{16}$$

where ζ is the ratio of inelastic to total electron energy losses (typically $\zeta \approx 220$). The lower limit on frequency for the homogeneous model occurs when $2\bar{s} = l$. For $\eta = 1$, this occurs in our simulations at 12 MHz. Choosing $\eta = 0.5$ in our simulation gives a lower limit of 6 MHz, consistent with the experiment. At 13.56 MHz, our simulation value of 370 A/m^2, for the discharge power of 8.6 W, lies within the range of current densities for stable α-mode operation, found to be 160–600 A/m^2.[14]

A simplified chemistry theoretical model was developed for the precursor generation in terms of a series reaction chain beginning with $TiCl_4$, with two reactive intermediate species, Ar^m and $TiCl_3$, producing the main precursor TiO_2Cl_3. The theory was compared with the simulation results, showing good agreement for the deposition rate versus time and the deposition rate versus discharge power. Our conclusion is that the simplified chemistry model is useful for understanding the scaling of deposition rates with discharge parameters.

The reaction set we used did not include the Ar_2^* excimer. We examined its importance using an extended reaction set, including the additional reactions $Ar^m + 2Ar \rightarrow Ar_2^* + Ar$, $Ar_2^* \rightarrow 2Ar + h\nu$, $Ar_2^* + Ar \rightarrow 3Ar$, $Ar_2^* + O_2 \rightarrow 2Ar + 2O$, $Ar_2^* + Ar^m \rightarrow 2Ar + Ar^+ + e$, and $Ar_2^* + TiCl_4 \rightarrow TiCl_3 + Cl + 2Ar$, with rate coefficients taken from the literature[33] (We used the rate coefficients of R102 and R176 for the last two reactions). Both at low and high O_2 fractions, we found almost no difference in the simulation results due to the excimer. This is not unexpected, as even at a low O_2 fraction of $f_{O_2} = 0.002$, the rate of metastable (Ar^m) generation of O and O^* (R104 and R105) is over three times the rate of Ar_2^* generation. At the higher O_2 fractions (e.g., $f_{O_2} = 0.129$ for the base case), the O and O^* generation far exceeds the excimer generation.

A significant weakness of the simulation is the absence of titanium-containing negative ion species. Including these species in the simulations, along with the buildup of heavy negative ion titanium species through processes such as (1), would be highly desirable as a first step in treating the possible formation of titanium-containing nanoparticulates in the discharge. There is some experimental evidences that these particulates may play a role in the deposition of these films.

ACKNOWLEDGMENTS

The authors thank A. J. Lichtenberg, C. Lazzaroni, and P. Chabert for their contributions in developing the simulation code used in this work. We also thank A. J. Lichtenberg and D. B. Graves for suggesting improvements to this MS. This work was partially supported by the Department of Energy Office of Fusion Energy Science Contract No. DE-SC000193 and by the Natural Science Foundation of China Contract Nos. 11375042 and 10835004.

APPENDIX: LAPLACE TRANSFORM SOLUTION

Equations (6) and (10)–(13) are solved by the method of Laplace transformation. The transform of n_{TiCl_4} is found to be

$$\mathcal{L}\left(\frac{n_{TiO_2}(t)}{n_{TiCl_4}(0)}\right) = \frac{\nu^3\nu_L}{(s+\nu_L)(s+\nu_W)(s+\nu)^3}, \tag{A1}$$

where s is the transform variable. Expanding in partial fractions gives

$$\mathcal{L}\left(\frac{n_{TiO_2}(t)}{n_{TiCl_4}(0)}\right) = \nu^3\nu_L\left[\frac{a_L}{s+\nu_L} + \frac{a_W}{s+\nu_W} + \frac{a_1}{s+\nu} + \frac{a_2}{(s+\nu)^2} + \frac{a_3}{(s+\nu)^3}\right], \tag{A2}$$

with

$$a_L = \frac{1}{(\nu_L-\nu)^3(\nu_L-\nu_W)}, \tag{A3}$$

$$a_W = \frac{1}{(\nu_W-\nu)^3(\nu_W-\nu_L)}, \tag{A4}$$

$$a_1 = \frac{\nu_L^2+\nu_W^2-3\nu_L\nu-3\nu_W\nu+\nu_L\nu_W+3\nu^2}{(\nu_L-\nu)^3(\nu_W-\nu)^3}, \tag{A5}$$

$$a_2 = \frac{2\nu-\nu_L-\nu_W}{(\nu_L-\nu)^2(\nu_W-\nu)^2}, \tag{A6}$$

$$a_3 = \frac{1}{(\nu_L-\nu)(\nu_W-\nu)}. \tag{A7}$$

Taking the inverse transform of (A2), we obtain the time-varying solution

$$\frac{n_{TiO_2}(t)}{n_{TiCl_4}(0)} = \nu^3\nu_L\left[a_L e^{-\nu_L t} + a_W e^{-\nu_W t} + \left(a_1 + a_2 t + \frac{1}{2}a_3 t^2\right)e^{-\nu t}\right]. \tag{A8}$$

[1]A. Fujishima and K. Honda, Nature **238**, 37 (1972).
[2]B. O'Regan and M. Grätzel, Nature **353**, 737 (1991).
[3]H. G. Yang, C. H. Sun, S. Z. Qiao, J. Zou, G. Liu, S. C. Smith, H. M. Cheng, and G. Q. Lu, Nature **453**, 638 (2008).
[4]R. X. Cai, Y. Kubota, T. Shuin, H. Sakai, K. Hashimoto, and A. Fujishima, Cancer Res. **52**, 2346 (1992).
[5]T. Paunesku, T. Rajh, G. Wiederrecht, J. Maser, S. Vogt, N. C. Stojićević, M. Protić, B. Lai, J. Oryhon, M. Thurnauer, and G. Woloschak, Nature Mater. **2**, 343 (2003).
[6]M. Grätzel, Nature **414**, 338 (2001).
[7]De X. Wang, "Preparation of 3D anatase titanium dioxide single crystal film via atmospheric pressure non-equilibrium plasma and Its luminescence study," Ph.D. thesis (In Chinese) (Donghua University, 2011).

[8]S. E. Pratsinis, H. Bai, P. Biswas, M. Frenklach, and S. V. R. Mastrangelo, J. Am. Ceram. Soc. **73**, 2158 (1990).
[9]F. Teyssandier and M. D. Allendorf, J. Electrochem. Soc. **145**, 2167 (1998).
[10]A. B. Murphy, J. Phys. D: Appl. Phys. **37**, 2841 (2004).
[11]R. H. West, M. S. Celnik, O. R. Inderwildi, M. Kraft, G. J. O. Beran, and W. H. Green, Ind. Eng. Chem. Res. **46**, 6147 (2007).
[12]R. H. West, G. J. O. Beran, W. H. Green, and M. Kraft, J. Phys. Chem. A **111**, 3560 (2007).
[13]R. H. West, R. A. Shirley, M. Kraft, C. F. Goldsmith, and W. H. Green, Combust. Flame **156**, 1764 (2009).
[14]J. Zhang, K. Ding, K. Wei, J. Zhang, and J. Shi, Phys. Plasmas **16**, 090702 (2009).
[15]C. Lazzaroni, P. Chabert, M. A. Lieberman, A. J. Lichtenberg, and A. Leblanc, Plasma Sources Sci. Technol. **21**, 035013 (2012).
[16]C. H. Lee, D. B. Graves, and M. A. Lieberman, Plasma Chem. Plasma Process. **16**, 99 (1996).
[17]T. Nakano and H. Sugai, J. Phys. D: Appl. Phys. **26**, 1909 (1993).
[18]X. Chen and D. W. Setser, J. Phys. Chem. **95**, 8473 (1991).
[19]E. G. Thorsteinsson and J. T. Gudmundsson, Plasma Sources Sci. Technol. **19**, 055008 (2010).
[20]R. B. Bird, W. E. Stewart, and R. N. Lightfoot, *Transport Phenomena*, 2nd ed. (Wiley-Interscience, New York, NY, 2002).
[21]J. Waskoenig, "Numerical simulations of the electron dynamics in single and dual frequency driven atmospheric pressure plasmas and associated plasma chemistry in electro-negative He-O_2 mixtures," Ph.D. thesis (Queens University of Belfast, 2010).
[22]J. Waskoenig, K. Niemi, N. Knake, L. M. Graham, S. Reuter, V. Schulz-von der Gathen, and T. Gans, Plasma Sources Sci. Technol. **19**, 045018 (2010).
[23]*Handbook of Tables for Applied Engineering Science*, 2nd ed., edited by R. E. Bolz and G. L. Tuve (CRC Press, Boca Raton, FL, 1973), p. 538.
[24]J. T. Gudmundsson and E. G. Thorsteinsson, Plasma Sources Sci. Technol. **16**, 399 (2007).
[25]C. Lazzaroni, P. Chabert, A. Rousseau, and N. Sadeghi, J. Phys. D: Appl. Phys. **43**, 124008 (2010).
[26]M. A. Lieberman and A. J. Lichtenberg, *Principles of Plasma Discharges and Materials Processing*, 2nd ed. (Wiley-Interscience, 2005).
[27]F. X. Bronold, K. Matyash, D. Tskhakaya, R. Schneider, and H. Fehske, J. Phys. D: Appl. Phys. **40**, 6583 (2007).
[28]E. G. Thorsteinsson and J. T. Gudmundsson, J. Phys. D: Appl. Phys. **43**, 115201 (2010).
[29]H. W. Ellis, R. Y. Pai, E. W. McDaniel, E. A. Mason, and L. A. Viehland, At. Data Nucl. Data Tables **17**, 177 (1976).
[30]D. X. Liu, M. Z. Rong, X. H. Wang, F. Iza, M. G. Kong, and P. Bruggeman, Plasma Processes Polym. **7**, 846 (2010).
[31]A. A. Fridman, L. Boufendi, T. Hbid, B. V. Potapkin, and A. Bouchoule, J. Appl. Phys. **79**, 1303 (1996).
[32]C. Lazzaroni, M. A. Lieberman, A. J. Lichtenberg, and P. Chabert, J. Phys. D: Appl. Phys. **45**, 495204 (2012).
[33]G.-B. Zhao, M. D. Argyle, and M. Radosz, J. Appl. Phys. **99**, 113302 (2006).